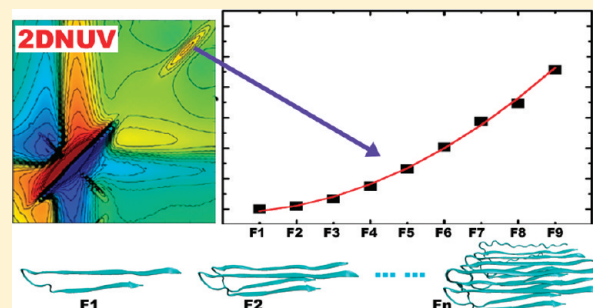


Probing Amyloid Fibril Growth by Two-Dimensional Near-Ultraviolet Spectroscopy

Jun Jiang* and Shaul Mukamel*

Chemistry Department, University of California, Irvine, Irvine, California 92697, United States

ABSTRACT: Keeping track of the aggregation kinetics of amyloid fibrils is essential for understanding their formation mechanism and eventually developing treatments for misfolded protein-related diseases. A simulation study of a series of $\text{A}\beta_{9-40}$ amyloid fibrils with different size shows that novel two-dimensional near-ultraviolet (2DNUV) spectra contain characteristic signatures of interactions between peptides. Chiral 2DNUV signals show a larger degree of exciton delocalization compared to their nonchiral counterparts. Intensities of specific peaks provide a direct measure of the number of peptides in a fibril. These signals could be used to monitor the fibril growth kinetics, one peptide at a time.



I. INTRODUCTION

Much attention has been directed to the formation and aggregation mechanisms of amyloid fibrils in misfolded proteins.^{1–5} These studies are motivated by the pursuit for effective cures to more than 20 neurodegenerative diseases.^{6–8} Water-soluble oligomeric forms of β -amyloid ($\text{A}\beta$) are believed to be the principal causes of the neurotoxicity in Alzheimer's disease. The step-by-step tracking of amyloid formation is thus most valuable. Important open issues are how the oligomer structure depends on aggregate size, how it affects amyloid formation, and how to characterize their physical and chemical properties. Recent progress made by identifying the oligomeric forms of $\text{A}\beta$, such as the monomer⁹ and dimer,^{10,11} could facilitate future studies of the aggregation mechanism.

Experimental tools for monitoring the oligomer size are required for tracking the amyloid formation.^{12–14} X-ray diffraction is not adequate since the fibrils do not form crystals. Optical spectroscopic techniques are good candidates. Conventional one-dimensional (1D) spectroscopy techniques such as circular dichroism (CD) and Raman have a limited resolution. Coherent multidimensional nonlinear optical spectra in contrast can reveal more detailed information about the fibril structure and kinetics of misfolded peptides.^{15–20} Two-dimensional IR spectroscopy (2DIR) with site-specific isotope labeling has been successfully utilized to track the amyloid formation pathway with residue-specific resolution.^{21,22} Our theoretical work had demonstrated that 2DIR signals allow a direct characterization of fibril aggregation pathways.²³

Recent advances in laser technology had made it possible to extend the multidimensional techniques into the near-ultraviolet (NUV) regime.^{24–29} Two dimensional near-ultraviolet (2DNUV) spectroscopy of proteins carries information on electronic excitations of aromatic side chains: phenylalanine (Phe), tyrosine (Tyr), and tryptophan (Trp). Since aromatic residues in proteins

are relatively rare, their spectra are site-specific and easier to characterize without isotope labeling. Electronic excitations of chromophores depend on their surroundings through electrostatic interactions, making them good local probes for the structure. By exploiting the high sensitivity of 2DNUV signals to interactions among protein residues and between peptides, the technique offers a powerful high-resolution local window for observing the size of amyloid fibrils.^{20,30,31}

In this paper, we employ our recently developed Quantum Mechanics/Molecular Mechanics (QM/MM) approach³¹ toward the simulation of 2DNUV spectra of a family of fibrils made of the 32-residue β -amyloid ($\text{A}\beta_{9-40}$) peptide. It has been shown that this segment is the key for fibril formation. We find that these spectra are sensitive to the interactions between neighboring peptides. We further show that 2DNUV may be used to monitor the number of peptides in an aggregated fibril and can thus probe the amyloid fibril formation kinetics.

II. SIMULATION DETAILS

In the case of Alzheimer's disease, fibrils are composed of β -amyloid ($\text{A}\beta$) peptides with 39–42 residues, which are rich in β -sheet secondary structure. Tycko and co-workers³² have proposed a molecular model for the conformation of $\text{A}\beta_{1-40}$. Since it is known that residues 1–8 are structurally disordered and not essential for the fibril growth,³³ we used the $\text{A}\beta_{9-40}$ fragment to model a single amyloid peptide. This contains three aromatic side chains: Tyr10, Phe19, and Phe20. MM simulations were carried out on the STAG(+2) structure composed of 12 $\text{A}\beta_{9-40}$ monomers, using the software package NAMD 2.7³⁴ with the CHARMM27³⁵ force field and the TIP3P water model³⁶.

Received: February 4, 2011

Revised: March 31, 2011

Published: April 25, 2011

as reported previously.³¹ We have harvested the central $\text{A}\beta_{9-40}$ peptide of the upper stack from the MM ensembles. This peptide was repeated to build a series of F_n fibrils with n periodically arrayed peptides, as shown in Figure 1. Ensembles of MM geometric snapshots of these amyloid fibrils were recorded for the UV studies.

We focused on the $^1\text{L}_a$ (~ 209 nm for Phe, ~ 216 nm for Tyr) and $^1\text{L}_b$ (~ 263 nm for Phe, ~ 274 nm for Tyr) electronic transitions. The transition energies and electric and magnetic dipole moments of isolated aromatic chromophores were calculated at the QM CASSCF/SCRF level (the complete-active space self-consistent field method implemented within a self-consistent reaction field in MOLCAS⁵⁷). We have applied the exciton Hamiltonian with the electrostatic fluctuations (EHEF) algorithm³¹ to calculate the electrostatic potential and inter- and intramolecular interactions. EHEF provides an interface for reading MM simulation trajectories from standard MD packages and generating QM atom–atom charge distributions. For a given conformation, charge distributions were deduced from standard atom–atom charges by updating atom–atom vectors of the corresponding MM geometric structure. These charge distributions were then used to calculate the electrostatic interactions between the chromophore and the explicit molecular environment. The fluctuating Hamiltonian was obtained at the QM level for all MD snapshots by avoiding expensive repeated QM calculations.³⁸ On the basis of the Frenkel exciton model, the matrix method in the DichroCalc code^{39,40} uses the EHEF parameters to construct the effective exciton Hamiltonian with electrostatic fluctuations. UV spectra are finally simulated using the SPECTRON code,⁴¹ by averaging over 1000 MM snapshots for 1D (linear absorption (LA) and CD) and 500 snapshots for 2D spectra.

2DNUV photon echo signals are generated by subjecting the system to four impulsive Gaussian laser pulses with carrier frequency $37\,000\text{ cm}^{-1}$ (270 nm) and full width at half-maximum (fwhm) 3754 cm^{-1} , as displayed in Figure 2 (A). The



Figure 1. Series of $\text{A}\beta_{9-40}$ amyloid fibrils F_n (with n peptides) studied in this work.

NUV CD and LA spectra of the fibril F_9 are displayed with arbitrary units in the same figure, showing that the laser power spectrum spans the absorption band in the NUV region. The four pulses in chronological order have wavevectors $\mathbf{k}_1, \mathbf{k}_2, \mathbf{k}_3$, and \mathbf{k}_4 . The three consecutive delay times are denoted t_1, t_2 , and t_3 . Setting t_2 to zero and using Fourier transform $t_1 \rightarrow \Omega_1$ and $t_3 \rightarrow \Omega_3$, we present two-dimensional correlation plots with respect to Ω_1 and Ω_3 .^{31,41} The 2D photon echo signals with $\mathbf{k}_4 = -\mathbf{k}_1 + \mathbf{k}_2 + \mathbf{k}_3$ were calculated using the protocol described earlier.³⁰ Signals are plotted on a nonlinear scale that clearly reveals both strong and weak features

$$\text{arcsinh}(cS) = \ln(cS + \sqrt{1 + c^2S^2}) \quad (1)$$

The signal S is first multiplied by a scale factor c to make its magnitude close to 1. For $cS < 1$ the scale is linear, $\text{arcsinh}(cS) \approx cS$, and for larger cS it becomes logarithmic, $\text{arcsinh}(cS) \approx (S|S|^{-1})\ln(2|cS|)$, so that weak features are amplified.

III. RESULTS

A. CD Spectra. The electronic spectra of the aromatic chromophores in proteins are sensitive to exciton couplings, which in turn depend on protein geometry.⁴² Simulated 1D CD spectra of amyloid fibril series F_1, F_2, F_4 , and F_9 are displayed in the bottom panel of Figure 2(B). Two experimental spectra are shown in the top panel (Exp1⁴³ and Exp2⁴⁴). The magnitude of the simulated mean residue ellipticity (ellipticity of the protein divided by the number of residues) is in good agreement with experiment. The simulated CD intensity closely resembles the latest experimental CD spectrum (exp1).⁴³ The negative feature observed in exp1 between $35\,000\text{ cm}^{-1}$ (286 nm) and $40\,000\text{ cm}^{-1}$ (250 nm) is reproduced by the simulations. The CD peaks in exp2 are sharper than in exp1 and in our simulations. Nevertheless, the main negative CD peaks in exp2 at $36\,200\text{ cm}^{-1}$ (276 nm), $37\,300\text{ cm}^{-1}$ (268 nm), and $38\,300\text{ cm}^{-1}$ (261 nm) are well reproduced by simulations for F_2, F_4 , and F_9 at $36\,500\text{ cm}^{-1}$ (274 nm), $37\,300\text{ cm}^{-1}$ (268 nm), and $38\,200\text{ cm}^{-1}$ (262 nm), with less than 2 nm shifts. The negative peaks at $37\,300\text{ cm}^{-1}$ (268 nm) and $38\,300\text{ cm}^{-1}$ (261 nm) are missing in the CD spectrum of F_1 , suggesting that they originate from interactions between peptides.

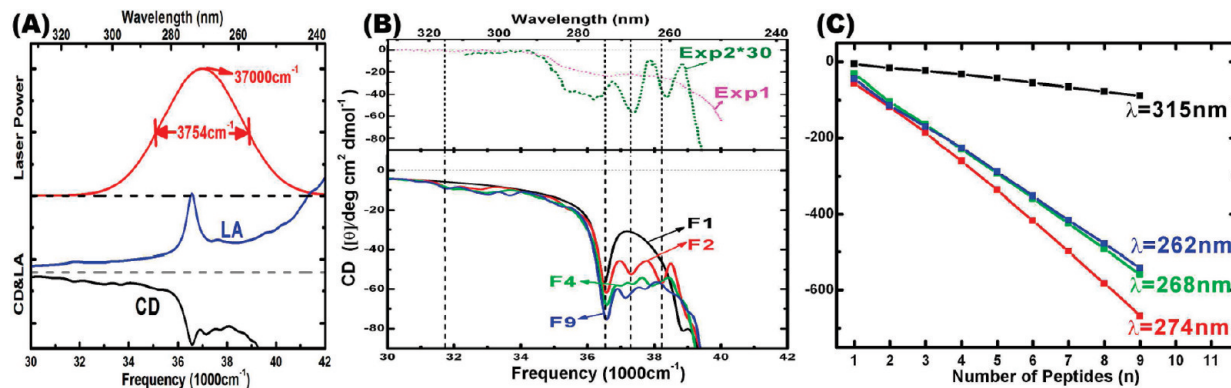


Figure 2. (A) Gaussian shape laser pulse power spectrum and NUV CD and LA spectra (linear scale and arbitrary unit) of the fibril F_9 below. The absorption band in the NUV region is covered by the pulse bandwidth. (B) (Bottom) Simulated NUV CD (mean residue ellipticity) spectra (bottom) of F_1, F_2, F_4 , and F_9 $\text{A}\beta_{9-40}$ fibrils. (Top) Two experimental spectra: Exp1⁴³ and Exp2⁴⁴ (magnified $\times 30$). Dashed vertical lines mark the primary CD negative peaks. (C) Variation of intensities (ellipticity of the whole protein) of the four main CD peaks with the number of peptides n in F_n fibrils.

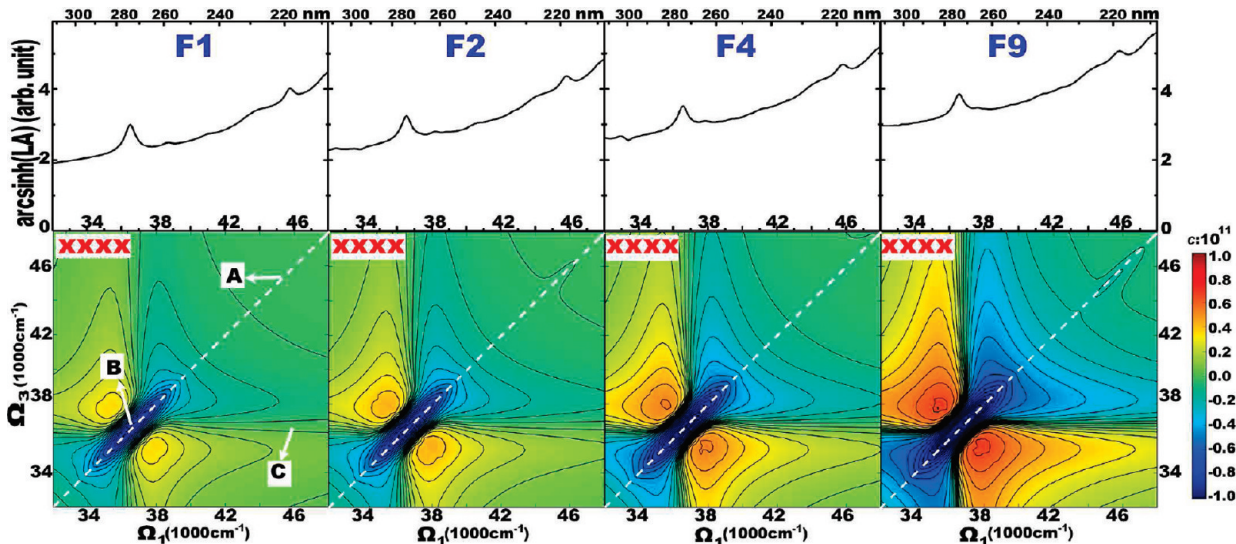


Figure 3. Simulated 2DNUV xxxx (bottom panel) spectra of fibrils F1, F2, F4, and F9 as marked. Linear absorption (LA) is given as top marginals. The scaling factor in eq 1 is $c = 10^{11}$. A and B label diagonal peaks at $46\ 500$ and $37\ 000\ \text{cm}^{-1}$, and C marks their cross-peak. White dashed lines mark the diagonal.

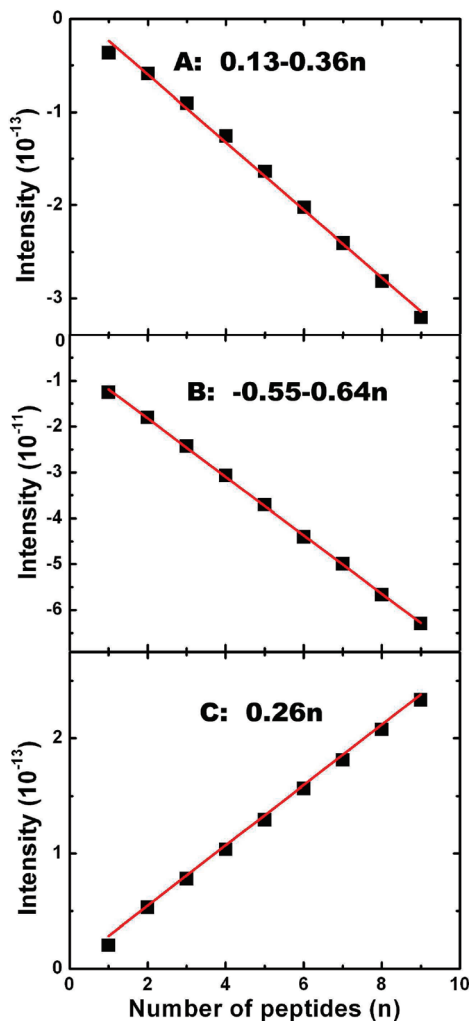


Figure 4. Variation of intensities of 2DNUV xxxx peaks A, B, and C with the number of peptides n in F_n fibrils.

Table I. Fitted a , b , and c Parameters of the Linear (Equation 2) or Parabolic (Equation 3) Functions of 2DNUV Signal as a Function of the Number of Peptides n in F_n Fibrils

signal	a	b	c
xxxx, A	0.13×10^{-13}	-0.36×10^{-13}	—
xxxx, B	-0.55×10^{-11}	-0.64×10^{-11}	—
xxxx, C	0	0.26×10^{-13}	—
xxxy, A	-1.23×10^{-18}	0	0.59×10^{-18}
xxxy, B1	25.19×10^{-17}	5.50×10^{-17}	-0.87×10^{-17}
xxxy, B2	-25.19×10^{-17}	5.50×10^{-17}	-0.87×10^{-17}
xxxy, C	-0.10×10^{-18}	-0.33×10^{-18}	—

We have used the ellipticity of the whole protein instead of the mean residue ellipticity, to compare CD intensities of fibrils with different size. The intensities of the four main CD peaks at wavelengths $\lambda = 262, 268, 274$, and $315\ \text{nm}$ (marked by dashed vertical lines in Figure 2(B)) grow linearly with the number of peptides n as seen in Figure 2(C), suggesting that the electronic transitions are localized within the peptide.

B. Nonchiral 2DNUV Signals. The simulated 2DNUV spectra of F1, F2, F4, and F9 for the nonchiral xxxx pulse polarization configuration³⁰ displayed in the bottom panel of Figure 3 show a similar pattern. The corresponding linear absorption (LA) spectra with the nonlinear scale (eq 1) are shown in the top panel. The ${}^1\text{L}_b$ and ${}^1\text{L}_a$ transitions show up as two LA peaks at $\sim 37\ 000$ and $46\ 500\ \text{cm}^{-1}$. These result in two diagonal peaks in the 2D spectra. Since we used Gaussian-shaped laser pulses centered at $37\ 000\ \text{cm}^{-1}$, the signals are dominated by the ${}^1\text{L}_b$ transitions, which show up as a negative (blue) diagonal peak (B) at $37\ 000\ \text{cm}^{-1}$ accompanied by two positive (red) side bands. A relatively weak negative (blue) ${}^1\text{L}_a$ diagonal peak (A) appears at $\sim 46\ 500\ \text{cm}^{-1}$. The cross-peak of A and B, marked C, is too weak to be observed.

The intensities of the A, B, and C peaks scale linearly with the number of peptides, as shown in Figure 4. As in Figure 2(B), this

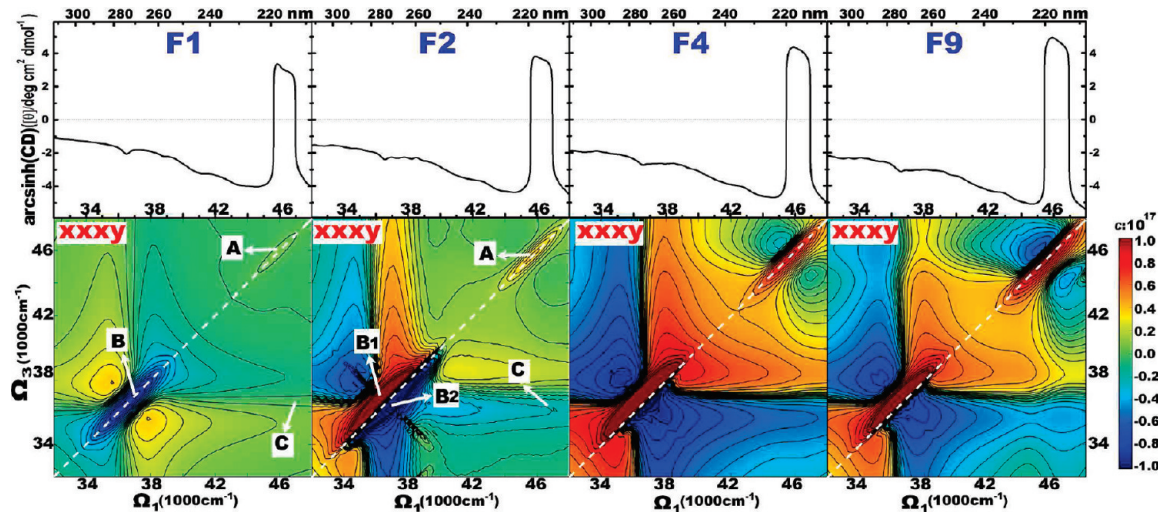


Figure 5. Simulated 2DNUV xxxxy (bottom panel) spectra of fibrils F1, F2, F4, and F9 as marked. CD spectra are given as top marginals. The scaling factor used in eq 1 is $c = 10^{17}$. A and B label diagonal peaks at $46\ 500$ and $37\ 000\ \text{cm}^{-1}$, and C marks their cross-peak. White dashed lines mark the diagonal.

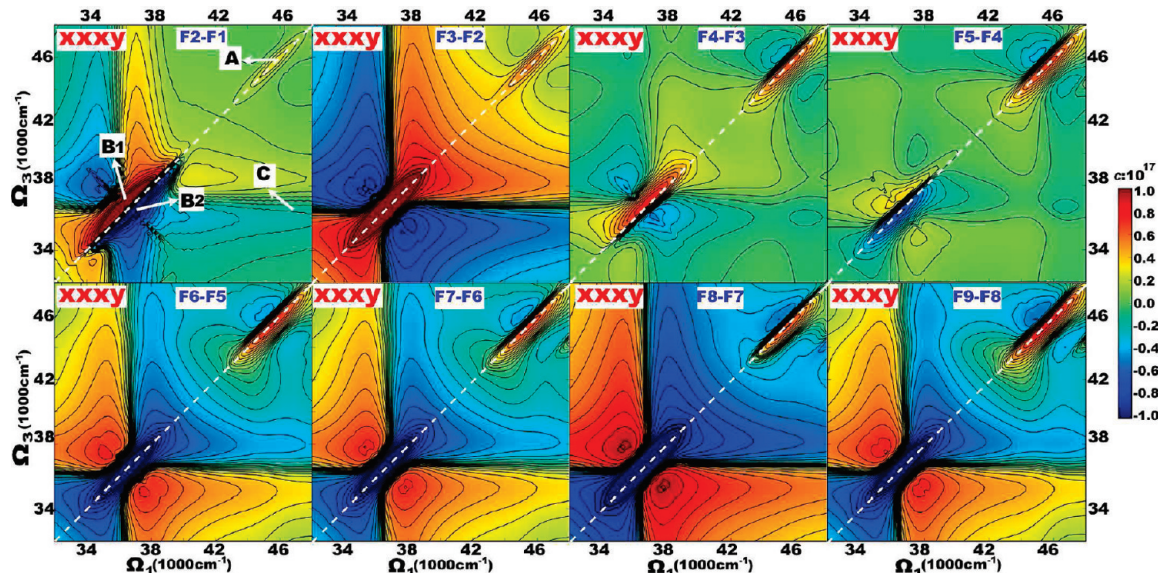


Figure 6. 2DNUV xxxxy difference spectra of F2–F1 to F9–F8. The scaling factor in eq 1 is $c = 10^{17}$. White dashed lines mark the diagonal.

suggests that the excitons are localized. The 2DNUV peak intensities for F1–F9 satisfy

$$S = a + bn \quad (2)$$

where b is the slope in Figure 4, and a accounts for edge effects in finite fibrils. The parameters a and b are listed in Table I. The finite a values for A and B come from interactions between peptides. We believe that these are limited to the nearest neighboring peptides. Peak C has $a = 0$, suggesting the interactions between peptides do not contribute to the cross-peak.

C. Chiral 2DNUV Signals. Our earlier studies^{20,30,31} had demonstrated that chirality-induced 2D signals are more sensitive to protein geometry and provide richer spectral features compared to their nonchiral counterparts. Simulated chiral 2DNUV xxxxy spectra of F1, F2, F4, and F9 fibrils are displayed in the bottom panel of Figure 5. The CD spectra on the top are

given as marginals. CD signals induced by ${}^1\text{L}_a$ and ${}^1\text{L}_b$ show up as the positive and negative peaks at $37\ 000$ and $46\ 500\ \text{cm}^{-1}$, respectively. These correspond to peaks A and B in the diagonal region of $46\ 500$ and $37\ 000\ \text{cm}^{-1}$, respectively. Here again peak B is enhanced by the laser pulse power spectrum centered at $37\ 000\ \text{cm}^{-1}$. The coupled ${}^1\text{L}_a/{}^1\text{L}_b$ transitions produce cross-peak C. Unlike the nonchiral spectra, here the spectral pattern does change with fibril size. Difference spectra of $\text{Fn} + 1 - \text{Fn}$ are shown in Figure 6.

Moving from F1 to F9, peak A (${}^1\text{L}_a$ transitions) retains the same pattern: a positive (red) diagonal peak accompanied by two negative (blue) side bands, while the signal intensities increase monotonically. The rise of signal A can be seen in the difference spectra of F2–F1 to F9–F8, which increase with fibril size. Peak A intensities in F1 to F9 fibrils plotted in Figure 7(A) show quadratic variation with n , unlike the linear dependence found for nonchiral xxxx signals.

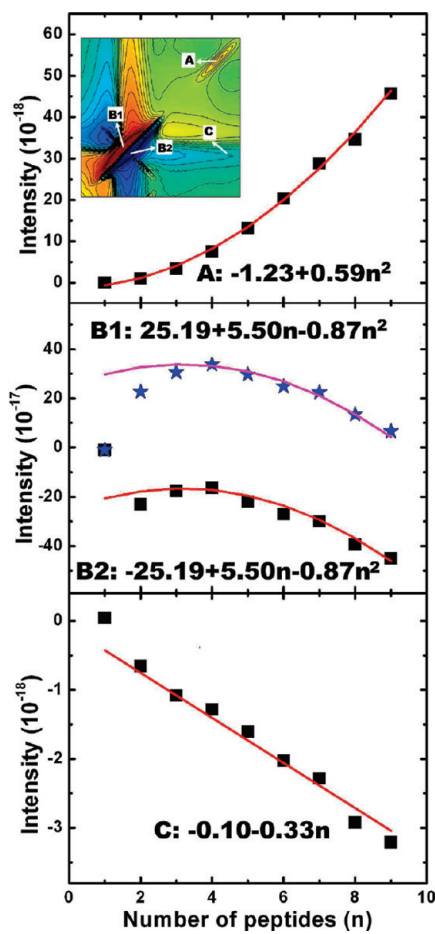


Figure 7. Variation of intensities of 2DNUV xxxy peaks A, B1 and B2, and C with the number of peptides n in F_n fibrils. A, B1, B2, and C peak locations are given in the 2DNUV xxxy signal of a dimer fibril F2 shown in the inset 2D graph of (A).

The variation of signal B (1L_b transitions) with fibril size is more complex. In F1 it is dominated by a negative (blue) diagonal peak which is symmetric across the diagonal. Proceeding from F1 to F2, the negative (blue) diagonal peak is split into a positive (red) and a negative (blue) peak in the upper and lower triangle region, labeled B1 and B2 in Figure 5, respectively. Correspondingly, the diagonal slice of F2 consists of one positive and one negative peak. The difference signals of F2–F1 given in Figure 6 suggest that interactions between two adjacent peptides produce B1 and B2. In the F3–F2 and F4–F3 difference spectra, the 1L_b region is dominated by a positive (red) diagonal peak. Consequently, the upper positive peak B1 becomes stronger, while the lower negative peak B2 becomes weaker as we move from F2 to F4 in Figure 5. A strong negative (blue) diagonal peak appears in the B region in F5–F4, which maintains the pattern and becomes dominant in F6–F5, F7–F6, F8–F7, and F9–F8, as shown in Figure 6. Because of this, the xxxy signal of F9 in Figure 5 has one strong B1 and one weak B2 peak, accompanied by two negative side bands. The positive peak of 1L_b transitions in the diagonal slice of F9 is lower than that of F4, meaning that the B1 peak in 2D spectra is decreasing with the increase of fibril size. The peak intensities of B1 and B2 displayed in Figure 7(B) show that the size variation is parabolic, F1 being an exception. The extreme points (with the highest intensity) of B1 and B2 occur at

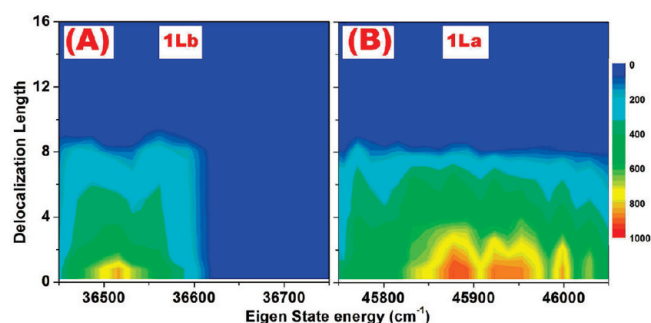


Figure 8. (A) and (B): Distribution of coherence lengths (L_c in eq 4) of the exciton eigen wave function of 1L_b and 1L_a transitions in the F16 fibril.

F4, instead of F1 or F2. This suggests that interactions between neighboring peptides saturate only beyond F4.

The variation of the chiral 2DNUV diagonal peaks with fibril size n is parabolic

$$S = a + bn + cn^2 \quad (3)$$

c represents the delocalization of exciton states; b accounts for the localized contributions; and a represents the edge effect. The computed xxxy signals A and B of fibrils up to F9 are well reproduced by the fitted parabolic curves in Figure 7(A) and (B). Since signal B becomes stable only beyond F4, we have excluded F1, F2, and F3 in fitting for signal B. The coherence length of delocalized 1L_a and 1L_b transitions in fibrils exceeds nine peptides. The coefficients a , b , and c are listed in Table I. For A, $b = 0$, implying that the chiral signals induced by 1L_a transitions are delocalized. B1 and B2 have nonzero b , suggesting the existence of localized contributions. Our previous study³¹ showed that the 1L_b transitions are strongly affected by the intramolecular interactions of three aromatic chromophores in the same peptide. We have also found that xxxy peak B induced only by one Tyr or Phe chromophore in each peptide has no linear b term. We therefore believe that the localized parts of signal B1 and B2 originate from intramolecular interactions between chromophores in the same peptide. The difference spectra of F6–F5 to F9–F8 shown in Figure 6 reveal that the evolutions of signals B1 and B2 are dominated by the increase of a symmetric negative (blue) diagonal peak. This explains why they possess the same b and c values.

The cross-peaks C between the ${}^1L_a/{}^1L_b$ transitions in F1, F2, and F4 of Figure 5 are very weak, but they may be observed in F9. These signals are clearly resolved in the difference spectra of Figure 6. For peak C, fibrils F2–F9 show linear size dependence in Figure 7(C), while F1 deviates from this trend. It is interesting to see that cross-peak C has linear scaling and is therefore localized. Most likely, the cross-peak is induced by the coupled ${}^1L_a/{}^1L_b$ transitions of the same aromatic chromophore. As discussed above, the interaction between chromophores in the same peptide normally produces localized signals. We expect that the coupled ${}^1L_a/{}^1L_b$ transitions of the same chromophore should also be localized. The fitted red line based on eq 2 is displayed in Figure 7, which explains very well fibrils F2–F9, but not F1. This suggests that interactions inside a trimer still contribute. The fitted linear coefficients in eq 3 are given in Table I.

D. Exciton Delocalization Underlying the 2DNUV Signals.

The exciton eigen-state e is a superposition of localized chromophore n . To connect 2DNUV spectral features to the transition

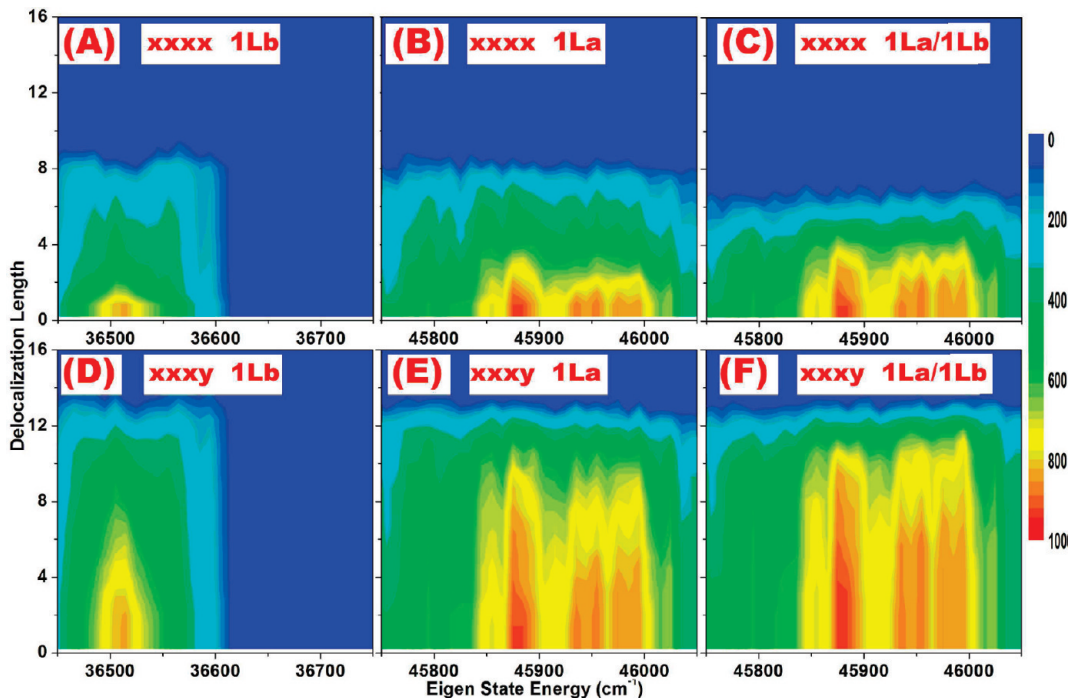


Figure 9. Distribution of the coherence lengths of nonchiral (top panel, $L_{e1,e2,NC}$ in eq 7) and chiral (bottom panel, $L_{e1,e2,CH}$ in eq 10) 2DNUV signals induced by 1L_b , 1L_a and coupled $^1L_a/^1L_b$ transitions as marked in the F16 fibril.

populations of aromatic side chains, we first examined the populations of exciton wave functions ($\psi_{e,n}$)². A good measure of the coherence (delocalization) length of 2DNUV signals is provided by the participation ratio⁴⁵

$$L_e = \left(\sum_n (\psi_{e,n})^2 \right)^{-1} \quad (4)$$

The distribution of delocalization length for different eigen-state energy is plotted in Figure 8. Most eigen-states are delocalized over four to six peptides.

The different size scaling of nonchiral and chiral signals can be rationalized by examining the origin of UV responses. The nonchiral response is induced by the transition dipoles of the zero-moment excited states, based on the dipole approximation which assumes that the optical fields are uniform across the molecules. On the other hand, chiral signals record interferences among transitions at different parts of molecules and reflect variations of the phase of optical fields at different points. Our previous work⁴⁶ showed that nonchiral response S_{NC} depends on the average product of exciton transition dipoles and the wave functions

$$S_{NC}^e \sim \sum_{m,n} |\psi_{e,m} \psi_{e,n} \mu_{e,m} \mu_{e,n}| \quad (5)$$

where m (n) denotes local chromophores, and $\psi_{e,m}$ and $\mu_{e,m}$ ($\psi_{e,n}$ and $\mu_{e,n}$) are the wave function and transition dipole of the eigen-state e , respectively. Consequently, the nonchiral 2D signal originating from chromophore n can be estimated by

$$S_{NC,2D}^{e1,e2,n} \sim \left(\sum_m |\psi_{e1,m} \psi_{e2,n} \mu_{e1,m} \mu_{e2,n}| \right)^2 \quad (6)$$

We can then calculate the coherence length of nonchiral 2DNUV

signals using the following participation ratio

$$L_{e1,e2,NC} = \left(\sum_n \left(\frac{S_{NC,2D}^{e1,e2,n}}{\sum_n S_{NC,2D}^{e1,e2,n}} \right)^2 \right)^{-1} \quad (7)$$

With two identical eigen-state energies $e_1 = e_2$, we have computed the coherence length of nonchiral (xxxx) diagonal peaks A (1L_a) and B (1L_b). That of the nonchiral (xxxx) cross-peak C ($^1L_a/^1L_b$ transitions) has also been computed, by setting eigen-states e_1 and e_2 corresponding to 1L_a and 1L_b transitions, respectively. The distribution of coherence lengths of xxxx signals in F16 is displayed as a function of energy e_1 in Figure 9(A), (B), and (C). The coherence lengths of 1L_b and 1L_a transitions induced xxxx signals displayed in Figure 9(A) and (B) are typically less than eight peptides and averaged at around four, while that of coupled $^1L_a/^1L_b$ cross-peaks as shown in Figure 9(C) is three. Compared to the eigen-states displayed in Figure 8, nonchiral signals have similar localization effects. This suggests that the contributions of intermolecular couplings decay quickly with increasing peptide–peptide distance and demonstrates the localized behavior of nonchiral 2DNUV signals.

Chiral signals are much weaker than their nonchiral counterparts. In 2D spectroscopy, chiral signals can be measured if nonchiral signals (the leading dipole contributions) are eliminated by laser pulses with an odd number of nonparallel polarization configurations (e.g., xxxy). The chiral response S_{CH} can then be estimated from²³

$$S_{CH}^e \sim \sum_{m,n} |\psi_{e,m} \psi_{e,n} \mathbf{R}_{mn} \cdot (\mu_{e,m} \times \mu_{e,n})| \quad (8)$$

where \mathbf{R}_{mn} is the displacement vector between the position of

the two transition dipoles $\mu_{e,m}$ and $\mu_{e,n}$. Because of the R_{mn} term, chiral signals could be much more delocalized than the nonchiral ones. Therefore, the chiral 2D signals of chromophore n can be evaluated from

$$S_{\text{CH}, 2D}^{e1, e2, n} \sim \left(\sum_m |\psi_{e1, m} \psi_{e2, n} R_{mn} \cdot (\mu_{e1, m} \times \mu_{e2, n})| \right)^2 \quad (9)$$

We can thus calculate the coherence length of chiral signals using the participation ratios

$$L_{e1, e2, \text{CH}} = \left(\sum_n \left(\frac{S_{\text{CH}, 2D}^{e1, e2, n}}{\sum_n S_{\text{CH}, 2D}^{e1, e2, n}} \right)^2 \right)^{-1} \quad (10)$$

The distributions of coherence lengths of chiral (xxxy) 2DNUV signals in F16 are displayed in Figure 9(D), (E), and (F), corresponding to 1L_b , 1L_a , and $^1L_a/{}^1L_b$ transitions, respectively. Obviously, chiral signals are much more delocalized than eigenstates displayed in Figure 8. The coherence lengths of xxxy signals have an average at around nine peptides for 1L_b and ten peptides for 1L_a . The same average coherence lengths have been obtained in transition population analysis of F20. This enables us to establish the coherence lengths of chiral 2DNUV diagonal signals in amyloid fibrils as nine to ten peptides. However, the average coherence lengths of xxxy $^1L_a/{}^1L_b$ cross-peaks are found to be ten peptides in F16 and eleven peptides in F20, suggesting that they are delocalized as well. This is inconsistent with their linear scaling behavior, which we believe is due to the neglect of the effect of mismatched eigen-state energies (i.e., $|e_1 - e_2| \gg 0$) in eq 9. The energy differences between 1L_b and 1L_a transitions are about $10\,000\text{ cm}^{-1}$, so the correlations in the cross-peaks should be much more localized than those induced by two identical transitions in the diagonal peaks.

IV. DISCUSSION

We have employed a QM/MM protocol, to simulate the CD and 2DNUV spectra of a series of 32-residue β -amyloid ($A\beta_{9-40}$) fibrils with a different number of peptides. Good agreement with experimental CD spectra validates our protocol. 2DNUV signals induced by the 1L_a , 1L_b , and coupled $^1L_a/{}^1L_b$ transitions of the aromatic side chains in fibrils show that they are sensitive to the interactions between neighboring peptides and are good indicators of size.

Interactions between peptides contribute to the nonchiral and chiral 2DNUV signals in a different way, leading to different size dependencies. We found that the coherence (delocalization) length of nonchiral 2D response is about four peptides for diagonal signals and three peptides for cross-peaks. Due to their localized nature, nonchiral 2DNUV signals grow linearly with fibril size. The 1L_a or 1L_b transition-induced signals mainly come from two structural elements: monomers and dimers. Signals induced by coupled $^1L_a/{}^1L_b$ transitions are even more localized, as the intermolecular interactions between peptides hardly contribute.

Since the coherence length of chiral 2D response is found to be nine to ten peptides, the chirality-induced 2DNUV signals in F1–F9 show nonlinear dependence on the fibril size. Signals produced by 1L_a transition grow quadratically in fibrils from one to nine peptides, indicating that the coherence length exceeds nine. For fibrils smaller than F4, the evolution of signals produced by 1L_b transitions is not as simple since the spectral

pattern varies. For larger fibrils, 1L_b signals show both parabolic and linear size dependence. The quadratic term represents delocalized intermolecular interactions, and the linear term results from the localized intramolecular interactions of aromatic chromophores in the same peptide. In contrast, signals induced by coupled $^1L_a/{}^1L_b$ transitions have linear size scaling as expected for transitions localized on three peptides.

The fact that 2DNUV signals induced by different transitions and interactions of various structural elements have a different scaling with size should be useful for probing fibril size. A linear or a quadratic formula represents very well the size dependencies of most 2DNUV signals in amyloid fibrils and can distinguish signals induced by different mechanisms. Using the coefficients tabulated here, the number of peptides can be calculated by comparing the intensities of different signals. The fibril aggregation kinetics can thus be monitored with a single-peptide resolution.

■ AUTHOR INFORMATION

Corresponding Author

*E-mail: jiang1@uci.edu; smukamel@uci.edu.

■ ACKNOWLEDGMENT

We gratefully acknowledge the support of the National Institutes of Health (Grant GM059230 and GM091364) and the National Science Foundation (Grant CHE-1058791).

■ REFERENCES

- (1) Rishton, G. M. Aggregator compounds confound amyloid fibrillation assay. *Nat. Chem. Biol.* **2008**, *4*, 159–160.
- (2) Feng, B. Y.; Toyama, B. H.; Wille, H.; Colby, D. W.; Collins, S. R.; May, B. C. H.; Prusiner, S. B.; Weissman, J.; Shiochet, B. K. Small-molecule aggregates inhibit amyloid polymerization. *Nat. Chem. Biol.* **2008**, *4*, 197–199.
- (3) Chiti, F.; Dobson, C. M. Amyloid formation by globular proteins under native conditions. *Nat. Chem. Biol.* **2009**, *5*, 15–22.
- (4) Fu, L.; Ma, G.; Yan, E. C. Y. In situ misfolding of human islet amyloid polypeptide at interfaces probed by sum frequency generation. *J. Am. Chem. Soc.* **2010**, *132*, 5405–5412.
- (5) Bleiholder, C.; Dupuis, N. F.; Wyttenbach, T.; Bowers, M. T. Ion mobility-mass spectrometry reveals a conformational conversion from random assembly to *b*-sheet in amyloid fibril formation. *Nature Chem.* **2011**, *3*, 172–177.
- (6) Tycko, R. Progress towards a molecular-level structural understanding of amyloid fibrils. *Curr. Opin. Struct. Biol.* **2004**, *14*, 96–103.
- (7) Caughey, B.; Lansbury, P. T. Protofibrils, pores, fibrils, and neurodegeneration: Separating the responsible protein aggregates from the innocent bystanders. *Annu. Rev. Neurosci.* **2003**, *26*, 267–298.
- (8) Lester-Coll, N. E.; Riviera, E. J.; Soscia, S. J.; Doiron, K.; Wands, J. R.; de la Monte, S. M. Intracerebral streptozotocin model of type 3 diabetes: Relevance to sporadic Alzheimer's disease. *J. Alzheimers Dis.* **2006**, *9*, 13–33.
- (9) Sandberg, A.; Luheshi, L. M.; Sölvander, S.; Pereira de Barros, T.; Macao, B.; Knowles, T. P.; Biverstål, H.; Lendel, C.; Ekholm-Petterson, F.; Dubnovitsky, A.; Lannfelt, L.; Dobson, C. M.; Härd, T. Stabilization of neurotoxic Alzheimer amyloid-beta oligomers by protein engineering. *Proc. Natl. Acad. Sci. U.S.A.* **2010**, *107*, 15595–15600.
- (10) O'Nuallain, B.; Freir, D. B.; Nicoll, A. J.; Risse, E.; Ferguson, N.; Herron, C. E.; Collinge, J.; Walsh, D. M. Amyloid beta-protein dimers rapidly form stable synaptotoxic protofibrils. *J. Neurosci.* **2010**, *30*, 14411–14419.

- (11) Wei, G.; Jewett, A. I.; Shea, J.-E. Structural diversity of dimers of the alzheimer amyloidbeta(25–35) peptide and polymorphism of the resulting fibrils. *Phys. Chem. Chem. Phys.* **2010**, *12*, 3622–3629.
- (12) Fawzi, N. L.; Yap, E.-H.; Okabe, Y.; Kohlstedt, K. L.; Brown, S. P.; Head-Gordon, T. Contrasting disease and nondisease protein aggregation by molecular simulation. *Acc. Chem. Res.* **2008**, *41*, 1037–1047.
- (13) Shankar, G. M.; Li, S.; Mehta, T. H.; Garcia-Munoz, A.; Shepardson, N. E.; Smith, I.; Brett, F. M.; Farrell, M. A.; Rowan, M. J.; Lemere, C. A.; Regan, C. M.; Walsh, D. M.; Sabatini, B. L.; Selkoe, D. J. Amyloid-protein dimers isolated directly from Alzheimer's brains impair synaptic plasticity and memory. *Nat. Med.* **2008**, *14*, 837–842.
- (14) Bernstein, S. L.; Dupuis, N. F.; Lazo, N. D.; Wyttenbach, T.; Condron, M. M.; Bitan, G.; Teplow, D. B.; Shea, J.-E.; Ruotolo, B. T.; Robinson, C. V.; Bowers, M. T. Amyloid- β protein oligomerization and the importance of tetramers and dodecamers in the aetiology of Alzheimer's disease. *Nature Chem.* **2009**, *1*, 326–331.
- (15) Chung, H. S.; Ganim, Z.; Jones, K. C.; Tokmakoff, A. Transient 2D IR spectroscopy of ubiquitin unfolding dynamics. *Proc. Natl. Acad. Sci. U.S.A.* **2007**, *104*, 14237–14242.
- (16) Mukamel, S.; Abramavicius, D.; Yang, L.; Zhuang, W.; Schweigert, I. V.; Voronine, D. Coherent multidimensional optical probes for electron correlations and exciton dynamics: from NMR to X-rays. *Acc. Chem. Res.* **2009**, *42*, 553–562.
- (17) Bagchi, S.; Falvo, C.; Mukamel, S.; Hochstrasser, R. M. 2D-IR experiments and simulations of the coupling between amide-I and ionizable side chains in proteins: Applications to the villin headpiece. *J. Phys. Chem.* **2009**, *113*, 11260–11273.
- (18) Kim, Y. S.; Liu, L.; Axelsen, P. H.; Hochstrasser, R. M. Two-dimensional infrared spectra of isotopically diluted amyloid fibrils from $\text{A}\beta$ 40. *Proc. Natl. Acad. Sci. U.S.A.* **2008**, *105*, 7720–7725.
- (19) Zhuang, W.; Abramavicius, D.; Voronine, D. V.; Mukamel, S. Multidimensional ultrafast spectroscopy special feature: Simulation of two-dimensional infrared spectroscopy of amyloid fibrils. *Proc. Natl. Acad. Sci. U.S.A.* **2007**, *104*, 14233–14236.
- (20) Jiang, J.; Abramavicius, D.; Falvo, C.; Bulheller, B. M.; Hirst, J. D.; Mukamel, S. Simulation of two dimensional ultraviolet (2DUV) spectroscopy of amyloid fibrils. *J. Phys. Chem. B* **2010**, *114*, 12150–12156.
- (21) Strasfeld, D. B.; Ling, Y. L.; Shim, S. H.; Zanni, M. T. Tracking fiber formation in human islet amyloid polypeptide with automated 2D-IR spectroscopy. *J. Am. Chem. Soc.* **2008**, *130*, 6698–6699.
- (22) Shim, S.-H.; Gupta, R.; Ling, Y. L.; Strasfeld, D. B.; Raleigh, D. P.; Zanni, M. T. Twodimensional IR spectroscopy and isotope labeling defines the pathway of amyloid formation with residue-specific resolution. *Proc. Natl. Acad. Sci. U.S.A.* **2009**, *106*, 6614–6619.
- (23) Zhuang, W.; Sgourakis, N. G.; Li, Z. Y.; Garcia, A. E.; Mukamel, S. Discriminating early stage $\alpha\beta$ 42 monomer structures using chirality-induced 2dir spectroscopy in a simulation study. *Proc. Natl. Acad. Sci. U.S.A.* **2010**, *107*, 15687–15692.
- (24) Ajdarzadeh Oskouei, A.; Bram, O.; Cannizzo, A.; van Mourik, F.; Tortschanoff, A.; Chergui, M. Photon echo peak shift experiments in the uv: p-terphenyl in different solvents. *J. Mol. Liq.* **2008**, *141*, 118–123.
- (25) Ajdarzadeh Oskouei, A.; Bram, O.; Cannizzo, A.; van Mourik, F.; Tortschanoff, A.; Chergui, M. Ultrafast uv photon echo peak shift and uorescence up conversion studies of non-polar solvation dynamics. *Chem. Phys.* **2008**, *350*, 104–110.
- (26) Tseng, C.; Matsika, S.; Weinacht, T. C. Two-dimensional ultrafast fourier transform spectroscopy in the deep ultraviolet. *Opt. Express* **2009**, *17*, 18788–18793.
- (27) Beutler, M.; Ghotbi, M.; Noack, F.; Brida, D.; Manzoni, C.; Cerullo, G. Generation of high-energy sub-20 fs pulses tunable in the 250–310 nm region by frequency doubling of a high-power noncollinear optical parametric amplifier. *Opt. Lett.* **2009**, *34*, 710–712.
- (28) Corkum, P.; De Silvestri, S.; Nelson, K.A.; Riedle, E.; Schoenlein, R.W., Editors. *Ultrafast Phenomena XVI*; Springer: New York, 2009.
- (29) Selig, U.; Schleussner, C.-F.; Foerster, M.; Langhofer, F.; Nuernberger, P.; Brixner, T. Coherent two-dimensional ultraviolet (2d-uv) spectroscopy in fully noncollinear geometry. *Opt. Lett.* **2010**, *35*, 4178–4180.
- (30) Abramavicius, D.; Jiang, J.; Bulheller, B. M.; Hirst, J. D.; Mukamel, S. Simulation study of chiral two dimensional ultraviolet (2DUV) spectroscopy of the protein backbone. *J. Am. Chem. Soc.* **2010**, *132*, 7769–7775.
- (31) Jiang, J.; Mukamel, S. Two-dimensional near-ultraviolet spectroscopy of aromatic residues in amyloid fibrils: A first principles study. *Phys. Chem. Chem. Phys.* **2011**, *13*, 2394–2400.
- (32) Petkova, A. T.; Yau, W. M.; Tycko, R. Experimental constraints on quaternary structure in Alzheimer's beta-amyloid fibrils. *Biochemistry* **2006**, *45*, 498–512.
- (33) Buchete, N.-V.; Tycko, R.; Hummer, G. Molecular dynamics simulations of Alzheimer's -amyloid protofilaments. *J. Mol. Biol.* **2005**, *353*, 804–821.
- (34) Phillips, J. C.; Braun, R.; Wang, W.; Gumbart, J.; Tajkhorshid, E.; Villa, E.; Chipot, C.; Skeel, R. D.; Kalé, L.; Schulten, K. Scalable molecular dynamics with NAMD. *J. Comput. Chem.* **2005**, *26*, 1781–1802.
- (35) MacKerell, A. D., Jr.; Bashford, D.; Bellott, M.; Dunbrack, R. L., Jr.; Evanseck, J. D.; Field, M. J.; Fischer, S.; Gao, J.; Guo, H.; Ha, S.; Joseph-McCarthy, D.; Kuchnir, L.; Kuczera, K.; Lau, F. T. K.; Mattos, C.; Michnick, S.; Ngo, T.; Nguyen, D. T.; Prodhom, B.; Reiher, W., III; Roux, B.; Schlenkrich, M.; Smith, J. C.; Stote, R.; Straub, J.; Watanabe, M.; Wiorkiewicz-Kuczera, J.; Yin, D.; Karplus, M. All-atom empirical potential for molecular modeling and dynamics studies of proteins. *J. Phys. Chem. B* **1998**, *102*, 3586–3616.
- (36) Jorgensen, W. L.; Chandrasekhar, J.; Madura, J. D.; Impey, R. W.; Klein, M. L. Comparison of simple potential functions for simulating liquid water. *J. Chem. Phys.* **1983**, *79*, 926–935.
- (37) Aquilante, F.; De Vico, L.; Ferré, N.; Ghigo, G.; Malmqvist, P.-A.; Neogrády, P.; Pedersen, T. B.; Pitónák, M.; Reiher, M.; Roos, B. O.; Serrano-Andrés, L.; Urban, M.; Veryazov, V.; Lindh, R. Molcas 7: The next generation. *J. Comput. Chem.* **2009**, *31*, 224–247.
- (38) Jiang, J.; Abramavicius, D.; Bulheller, B. M.; Hirst, J. D.; Mukamel, S. Ultraviolet spectroscopy of protein backbone transitions in aqueous solution: Combined QM and MM simulations. *J. Phys. Chem. B* **2010**, *114*, 8270–8277.
- (39) Hirst, J. D Improving protein circular dichroism calculations in the far ultraviolet through reparametrizing the amide chromophore. *J. Chem. Phys.* **1998**, *109*, 782–788.
- (40) Bulheller, B. M.; Rodger, A.; Hirst, J. D. Circular and linear dichroism of proteins. *Phys. Chem. Chem. Phys.* **2007**, *9*, 2020–2035.
- (41) Abramavicius, D.; Palmieri, B.; Voronine, D. V.; Šanda, F.; Mukamel, S. Coherent multidimensional optical spectroscopy of excitons in molecular aggregates: quasiparticle, vs. supermolecule perspectives. *Chem. Rev.* **2009**, *109*, 2350–2408.
- (42) Rogers, D. M.; Hirst, J. D. First-principles calculations of protein circular dichroism in the near ultraviolet. *Biochemistry* **2004**, *43*, 11092–11102.
- (43) Tang, C.-H.; Zhang, Y.-H.; Wen, Q.-B.; Huang, Q. R. Formation of amyloid fibrils from kidney bean 7s globulin (phaseolin) at pH 2.0. *J. Agric. Food Chem.* **2010**, *58*, 8061.
- (44) Sian, A. K.; Frears, E. R.; El-Agnaf, O. M. A.; Patel, B. P.; Manca, M. F.; Siligardi, G.; Hussain, R.; Austen, B. M. Oligomerization of β -amyloid of the alzheimer's and the dutch-cerebral-haemorrhage types. *Biochem. J.* **2000**, *349*, 299–308.
- (45) Hayashi, T.; Mukamel, S. Vibration-exciton couplings for the amide i, ii, iii and a modes of peptides. *J. Phys. Chem. B* **2007**, *111*, 11032–11046.
- (46) Zhuang, W.; Hayashi, T.; Mukamel, S. Coherent multidimensional vibrational spectroscopy of biomolecules; concepts, simulations and challenges. *Angew. Chem., Int. Ed.* **2009**, *48*, 3750–3781.